Seismic Evidence for Sharp Lithosphere-Asthenosphere Boundaries of Oceanic Plates

Hitoshi Kawakatsu,[1]* Prakash Kumar,[1]† Yasuko Takei,[1] Masanao Shinohara,[1] Toshihiko Kanazawa,[1] Eiichiro Araki,[2] Kiyoshi Suyehiro[2]

The mobility of the lithosphere over a weaker asthenosphere constitutes the essential element of plate tectonics, and thus the understanding of the processes at the lithosphere-asthenosphere boundary (LAB) is fundamental to understand how our planet works. It is especially so for oceanic plates because their relatively simple creation and evolution should enable easy elucidation of the LAB. Data from borehole broadband ocean bottom seismometers show that the LAB beneath the Pacific and Philippine Sea plates is sharp and age-dependent. The observed large shear wave velocity reduction at the LAB requires a partially molten asthenosphere consisting of horizontal melt-rich layers embedded in meltless mantle, which accounts for the large viscosity contrast at the LAB that facilitates horizontal plate motions.

Oceanic plates are created at mid-oceanic ridges and spread away as a rigid body (lithosphere) to move over a weaker asthenosphere. The age of oceanic plate is recorded by the magnetic lineation, and its evolution is well explained by thermal cooling of a moving plate. The bottom of an oceanic plate was thought to correspond to the top of the seismically observed low-velocity layer around a depth of 50 to 100 km, possibly indicating the presence of partially molten mantle rocks (*1*), and the thickening of oceanic plates with the age has been confirmed by using low-resolution surface waves (*2*). An alternative is that the oceanic lithosphere is hardened by water extraction at the mid-oceanic ridges (*3*, *4*), and once the lithosphere is created it does not evolve nor thicken. In this case, the observed age dependence is solely a thermal effect. This view predicts that the seismic lithosphere-asthenosphere boundary (LAB) signal should be small [~1 to 2% velocity reduction (*3*)].

We detected the bottom of oceanic plates beneath the normal ocean by using high-resolution body waves observed by the borehole broadband ocean bottom seismometry. A LAB has been observed beneath continents (*5*, *6*). Attempts to observe the oceanic LAB by using long-period body waves that traverse long distance in the mantle suffers from the large spatial averaging and the contamination from highly heterogeneous structure at the bottom of the mantle. Data beneath normal oceans have been lacking because of the lack of high-quality ocean bottom broadband seismic observatories. Under the Japanese Ocean Hemisphere network Project (OHP) (*7*), ocean bottom broadband seismic observatories were deployed, and two borehole stations, WP1 and WP2, were operated for a few years in the Philippine Sea and the Pacific Ocean, respectively (Figs. 1 and 2) (*8*–*10*). We applied P- and S-receiver function (RF) techniques to the teleseismic data (*5*, *11*–*13*). The RF technique uses compression-to-shear (*P*-to-*S*, P-RF) and shear-to-compression (*S*-to-*P*, S-RF) converted seismic waves to detect sharp velocity changes beneath stations. The S-RF method is especially powerful for detecting signatures like LAB at depths between 50 and 200 km, for which strong signal-generated interfering phases are present in the P-RF method (*5*, *13*). Because the seismological observatories were situated at a depth of ~500 m below the ocean floor and below ~5-km-thick water column, we also had to properly estimate the effect of water

[1]Earthquake Research Institute, University of Tokyo, 1-1-1 Yayoi, Bunkyo-ku, Tokyo 113-0032, Japan. [2]Japan Agency for Marine-Earth Science and Technology, 2-15 Natsushima, Yokosuka, Kanagawa 237-0061, Japan.

*To whom correspondence should be addressed. E-mail: hitosi@eri.u-tokyo.ac.jp

†On leave from National Geophysical Research Institute, Uppal Road, Hyderabad-500007, India.

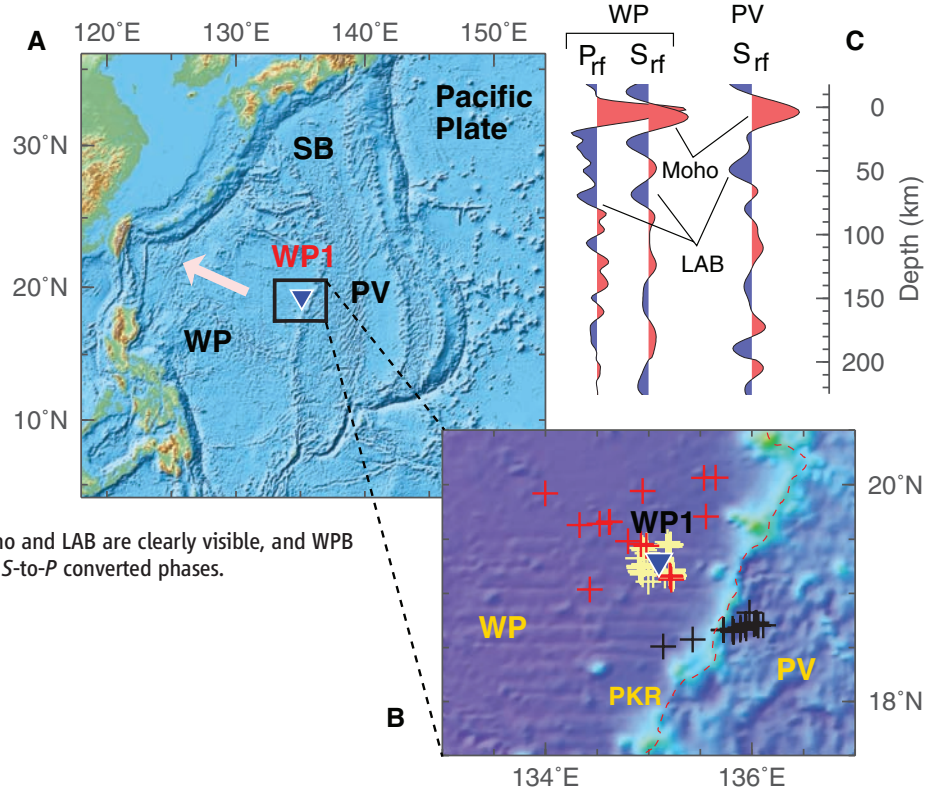

Fig. 1. Location of borehole broadband seismic observatory WP1 and the receiver functions. (**A**) The location of WP1 (inverted blue triangle) in the Philippine Sea plate. This station is at a depth of 561 m below seafloor with an ocean water thickness of 5710 m (*9*). (**B**) Zoomed version of the rectangular region around the station. Palau Kyushu Ridge (PKR) runs almost in the center of the Philippine Sea plate from north to south and divides the plate into two distinct geological provinces: PVB, Parece-Vela basin (15 to 27 My), and WPB, Western Philippine basin (33 to 49 My). Crosses in yellow and red are the piercing points for *P*-to-*S* and *S*-to-*P* converted waves, respectively, at 70 km depth falling in the WPB, whereas black crosses are the piercing points for *S*-to-*P* conversion falling mostly in the PVB. (**C**) Stacked radial P-RFs and S-RFs from WP1 for WPB and PVB. Red and blue colors indicate positive and negative values of RFs, respectively. Only *S*-to-*P* piercing points sample the PVB because of the larger *S*-wave slowness. Converted signals from Moho and LAB are clearly visible, and WPB shows the consistent structure with both *P*-to-*S* and *S*-to-*P* converted phases.

reverberations. Systematic modeling using synthetic waveforms show that S-RF is also an effective tool for such a case, whereas P-RF can be significantly disturbed by the presence of the ocean (*10*).

The results of RFs of two observatories show consistent findings (Figs. 1 to 3). The analyses reveal at least two prominent discontinuities present in the first 10 s of RFs (roughly corresponding to depths of 0 to 100 km beneath the station), one with positive polarity corresponding to the oceanic Moho, followed by a negative discontinuity, which we interpret as the LAB. Crustal phases in both regions are observed at a delay time of ~1 s, corresponding to 7- to 8-km-thick oceanic crusts that are close to the regionally determined estimates based on active seismic data (*9*) and to the global average.

The station WP1 in the central Philippine Sea is located near the Palau Kyushu Ridge (PKR), and observed S-RFs are grouped into two depending on the location relative to PKR of the piercing points of the LAB signals (Fig. 1B). The prominent phases corresponding to LAB occur at ~7.5 s (76 ± 1.8 km, 1 SE) for both P-RF and S-RF for piercing points located directly beneath the station, which is situated in the west of PKR with a plate age of ~49 million years (My). The same LAB phase was observed ~2 s earlier (~55 km LAB) for S-RF of eastern piercing points where the plate age is ~25 My. For WP2 in the northwestern Pacific ocean where the plate age is ~129 My, the data quality is slightly lower (*10*), but we still observe similar LAB phases at ~7–8 s for both P-RF and S-RF. The waveform modeling gives the best estimate for LAB depth of 82 ± 4.4 km (Fig. 3C). A deep LAB is also observed for the old Pacific plate beneath northeast Japan, where the highest quality seismic data are available from Japanese high-sensitivity seismograph network (Hi-net) to allow detailed imaging of subducting plate (*14*). The imaged thickness of the lithosphere is ~80 km (Fig. 2A) (*15*). Because the

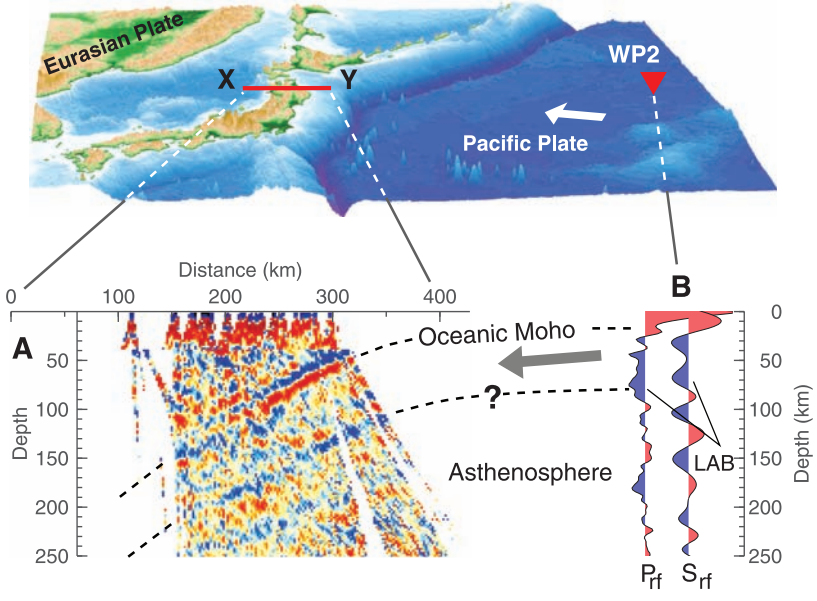

Fig. 2. RFs for WP2 and RF image of subducting Pacific plate beneath northeast Japan. In the topographic map, the inverted red triangle indicates the location of WP2, which is deployed at a depth of 460 m below the seafloor with a water column of 5566 m thick. (**A**) P-RF image along the profile XY using dense land seismic data of Hi-net from Japan (*10*). Red and blue colors indicate velocity increase (from shallow to deep) and decrease at the point, respectively. The top surface of the slab and the oceanic Moho are clearly imaged, as well as the bottom surface of the slab (i.e., subducting LAB). (**B**) P-RF and S-RF for WP2. Negative phases associated with a shear wave velocity drop marked as LAB appear to correspond to the strong negative (blue) signature of the subducting slab below Japan.

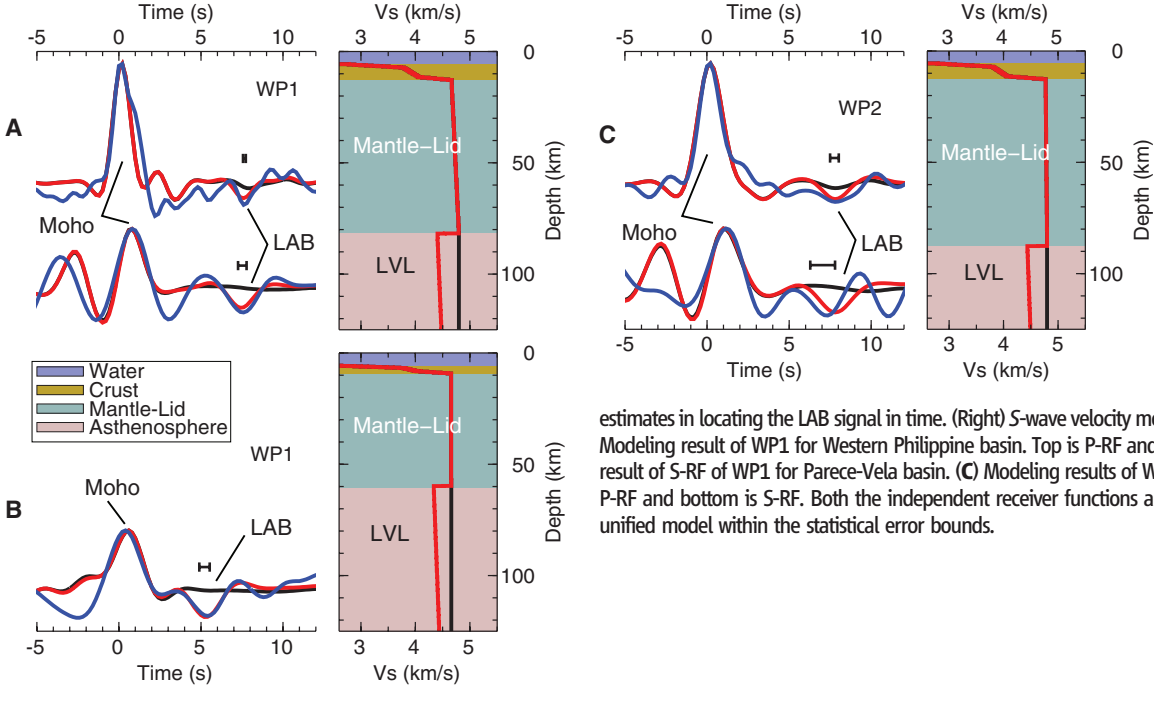

Fig. 3. Modeling of RFs for borehole seismological observatories. Blue lines indicate observed stacked receiver functions; black, the synthetic receiver functions for the model containing no low velocity layer (LVL); and red, synthetic receiver functions for the model shown on the right-hand graph with the same color. The horizontal lines just above the negative LAB phases are bootstrap error estimates in locating the LAB signal in time. (Right) *S*-wave velocity model used for synthetic RFs. (**A**) Modeling result of WP1 for Western Philippine basin. Top is P-RF and bottom is S-RF. (**B**) Modeling result of S-RF of WP1 for Parece-Vela basin. (**C**) Modeling results of WP2 for the Pacific plate. Top is P-RF and bottom is S-RF. Both the independent receiver functions are well matched with use of a unified model within the statistical error bounds.

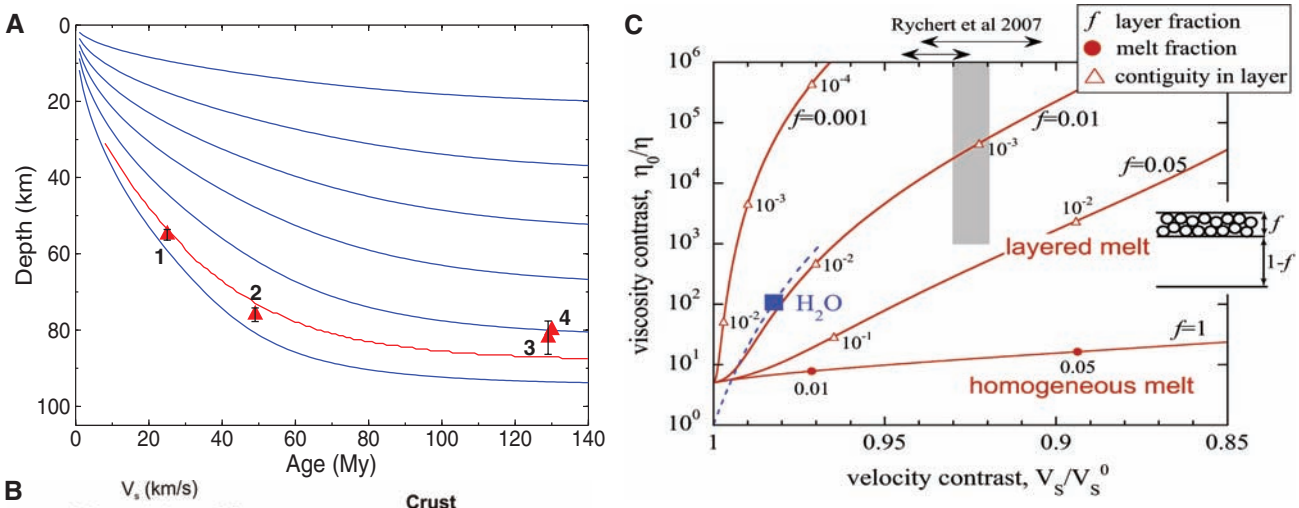

Fig. 4. Age dependence of observed LAB depths and a model for LAB and asthenosphere. (**A**) Observed LAB depths are plotted as a function of the plate age (red triangles; 1 indicates PVB; 2, WPB; 3, WP2; and 4, northeast Japan) over the isotherms given in a 200° intervals (blue lines) (*18*). Red line indicates the top of partial melting region calculated on the basis of the model of Mierdel *et al.* defined by the water solubility of 1000 parts per million H_2O (*16*). (**B**) A schematic illustration for the LAB and the asthenosphere. A schematic model for a *S*-wave seismic velocity structure of a radial anisotropy is superposed. (**C**) Viscosity (η) versus *S*-wave velocity (V_S) contrasts at LAB predicted from models of wet asthenosphere (bule) and partially molten asthenosphere (red), with seismological and geodynamical requirements (shaded) (*30*). Subscript 0 denotes lithospheric values. In the partially molten asthenosphere model, horizontal melt-rich layers are embedded in meltless mantle with various layer fractions from $f = 1$ (homogeneous) to $f = 0.001$. For $f = 1$ (homogeneous), melt has equilibrium geometry with variable melt fraction ϕ. For $f < 1$ (layered), ϕ in layers is close to the disaggregation melt fraction ϕ_c, and contiguity φ of grain-to-grain contact is small and variable [$\varphi = 1$ means melt-free and $\varphi = 0$ means disaggregation (*19*, *25*)]. Average ϕ in asthenosphere is given by $f\phi_c$.

age of subducting plate there is estimate to be ~130 My, the depth of 80 km for the LAB is consistent with that from the WP2 data.

The relative thickness of oceanic plates estimated above is consistent with the thermally controlled origin for the oceanic LAB (Fig. 4A), but the observation in short-period waves (~3 s) indicates that the LAB is a sharp boundary (the transition thickness of less than ~10 to 15 km) and thus has chemical or fabric origin. This apparent age dependence and the large LAB signal preclude the water-extraction model for the origin of oceanic LAB (*3*). One possibility to explain these features is partial melting in the asthenosphere. The depth of the initiation of the partial melting is estimated on the basis of the solubility of water in aluminous orthopyroxene component of mantle rocks (*16*–*18*). Although the fit is not perfect, this kind of model is capable of reproducing the basic trend in data (Fig. 4A).

Waveform modeling given in Fig. 3 indicates that the shear wave velocity is reduced at the LAB by ~7 to 8%. For a texturally equilibrated partially molten region, this translates into the melt fraction of ~3.5 to 4.0% (*19*), which is one order of magnitude larger than the commonly accepted amount of melt at mid-oceanic ridges (*20*) and may be unrealistically high. Therefore, some additional mechanism other than the conventional view of the partially molten asthenosphere is required.

Recent experimental and theoretical studies demonstrate that deformation can segregate melt into bands (*21*, *22*). On the basis of these results, we propose a model of partially molten asthenosphere consisting of horizontal melt-rich layers embedded in melt-less mantle (Fig. 4B). Such layered melt efficiently reduces vertically propagating shear wave velocities (*23*) and explains well the strong LAB signals reported here and elsewhere (*6*), as well as other properties expected for the asthenosphere. Figure 4C shows the velocity and viscosity contrasts at LAB predicted for a model of wet asthenosphere (blue), a conventional model of homogeneous partially molten asthenosphere (red line with layer fraction $f = 1$), and the present model of layered asthenosphere (red lines with $f < 1$). The strong seismological signals and a large viscosity contrast of $>10^3$ at LAB (*24*) can be explained quantitatively by the layered model, whereas the other two models cannot. The combination of both seismological and geodynamical constraints at the LAB (shaded) indicates that the melt-rich layers make up less than 5% by volume of the mantle here and that the melt fraction is close to the disaggregation melt fraction, ϕ_c, over which the partially molten rock loses grain-to-grain contacts (contiguity) and hence loses rigidity. Small but nonzero contiguity of the grains causing small rigidity of layers is important for the converted phases to be detectable. For $\phi_c = 0.25$ and $f = 0.05$ to 0.01, the average melt fraction in the asthenosphere is 1.25 to 0.25%, which is consistent with the petrological expectation (*20*). We describe the internal structure of the layers by grain-scale contiguity so that granular models developed recently to predict both elasticity and viscosity (*19*, *25*) can be applied. However, the obtained small rigidity of the layers might imply kinks and/or jogs, which may develop at much larger scales than grain size.

The layered model qualitatively explains other characteristics expected for the asthenosphere, such as radial anisotropy (transverse isotropy with a radial symmetry axis) inferred from long-period surface waves (*26*), high electrical conductivity (*27*), and high attenuation. The depth extent of this low-velocity asthenosphere is estimated to be ~210 km beneath WP2 on the basis of the travel-time analysis of WP2 data (*9*). Considering that LABs (*5*), the radial anisotropic layer (*28*), and the partially molten region (*16*) are all observed to be deeper (~200 km) beneath stable continents, the proposed model may be applicable to the continental asthenosphere to be an universal model for the asthenosphere.

References and Notes

1. B. Gutenberg, *Physics of the Earth's Interior* (Elsevier, New York, 1959).
2. H. Kanamori, F. Press, *Nature* **226**, 330 (1970).
3. S. Karato, H. Jung, *Earth Planet. Sci. Lett.* **157**, 193 (1998).
4. G. Hirth, D. Kohlstedt, *Earth Planet. Sci. Lett.* **144**, 93 (1996).
5. P. Kumar, X. Yuan, R. Kind, J. Ni, *J. Geophys. Res.* **111**, 10.1029/2005JB003930 (2006).
6. C. A. Rychert, K. M. Fischer, S. Rondenay, *Nature* **436**, 542 (2005).
7. Y. Fukao *et al*., in *Workshop Report of OHP/ION Joint Symposium, Long-Term Observations in the Oceans* (Earthquake Research Institute, Univ. of Tokyo, Tokyo, Japan, 2001), pp. 13–29.
8. M. Shinohara *et al*., *Ann. Geophys.* **49**, 625 (2006).
9. M. Shinohara *et al*., *Phys. Earth Planet. Inter.* **170**, 95 (2008).
10. Materials and methods are available as supporting material on *Science* Online.
11. L. P. Vinnik, *Phys. Earth Planet. Inter.* **15**, 39 (1977).
12. C. A. Langston, *J. Geophys. Res.* **84**, 4749 (1979).
13. V. Farra, L. Vinnik, *Geophys. J. Int.* **141**, 699 (2000).
14. H. Kawakatsu, S. Watada, *Science* **316**, 1468 (2007).
15. T. Tonegawa, K. Hirahara, T. Shibutani, N. Fujii, *Earth Planet. Sci. Lett.* **247**, 101 (2006).
16. K. Mierdel, H. Keppler, J. R. Smyth, F. Langenhorst, *Science* **315**, 364 (2007).
17. S. Honda, D. A. Yuen, *Geophys. Res. Lett.* **28**, 351 (2001).
18. The thermal model is constructed incorporating the pressure and temperature effect on the thermal diffusivity; among the range of models that give similar fit to surface observables (*29*), one with the plate thickness of 104 km and the temperature at the base of plate 1358°C (corresponding to a potential temperature of 1315°C) is used.
19. Y. Takei, *J. Geophys. Res.* **107**, 10.1029/2001JB000522 (2002).
20. J. Langmuir, E. M. Klein, T. Plank, in *Mantle Flow and Melt Generation at Mid-Ocean Ridges* (American Geophysical Union, Washington, DC, 1992), pp. 183–200.
21. B. K. Holtzman *et al*., *Science* **301**, 1227 (2003).
22. R. F. Katz, M. Spiegelman, B. Holtzman, *Nature* **442**, 676 (2006).
23. G. E. Backus, *J. Geophys. Res.* **67**, 4427 (1962).
24. M. Takaku, Y. Fukao, *Phys. Earth Planet. Inter.* **166**, 44 (2008).
25. Y. Takei, B. K. Holtzman, *J. Geophys. Res.*, in press.
26. G. Ekström, A. M. Dziewonski, *Nature* **394**, 168 (1998).
27. K. Baba, A. D. Chave, R. L. Evans, G. Hirth, R. L. Mackie, *J. Geophys. Res.* **111**, B02101 (2006).
28. Y. Gung, M. Panning, B. Romanowicz, *Nature* **422**, 707 (2003).
29. C. A. Stein, S. Stein, *Nature* **359**, 123 (1992).
30. In the wet asthenosphere model, the velocity contrast is estimated from the relation between η_0/η and V_S/V_S^0 (*3*) (blue dotted line) and $\eta_0/\eta \cong 100$ (*4*). In the partially molten asthenosphere model, viscosity of grain-boundary diffusion creep and elasticity are calculated for each layer by granular models (*19*, *25*), and effective properties of layered medium are calculated by the Backus average (*23*). In the layered model, η_0/η shows the contrast for horizontal shear flow, and V_S/V_S^0 shows the contrast of equivalent isotropic media, which give the same amplitude of *S*-to-*P* phase for the incident angle of 25° (typical for this study) (*10*).
31. B. Holtzman's drawing [figure 12 of (*25*)] was the inspiration for the proposed model of the melt-segregated shear zone in the asthenosphere. We thank S. Honda for the computer code to calculate the thermal structure and T. Inoue and K. Mibe for discussions. P.K. is supported by the JSPS fellowship provided by the Japan Society for the Promotion of Science. OHP was funded by the Ministry of Education, Culture, Sports, Science, and Technology of Japan.

Supporting Online Material

www.sciencemag.org/cgi/content/full/324/5926/499/DC1
Materials and Methods
Figs. S1 to S11
References

9 December 2008; accepted 26 February 2009
10.1126/science.1169499

Subducting Slab Ultra-Slow Velocity Layer Coincident with Silent Earthquakes in Southern Mexico

Teh-Ru Alex Song,[1]* Donald V. Helmberger,[2] Michael R. Brudzinski,[3] Robert W. Clayton,[2] Paul Davis,[4] Xyoli Pérez-Campos,[5] Shri K. Singh[5]

Great earthquakes have repeatedly occurred on the plate interface in a few shallow-dipping subduction zones where the subducting and overriding plates are strongly locked. Silent earthquakes (or slow slip events) were recently discovered at the down-dip extension of the locked zone and interact with the earthquake cycle. Here, we show that locally observed converted *SP* arrivals and teleseismic underside reflections that sample the top of the subducting plate in southern Mexico reveal that the ultra-slow velocity layer (USL) varies spatially (3 to 5 kilometers, with an *S*-wave velocity of ~2.0 to 2.7 kilometers per second). Most slow slip patches coincide with the presence of the USL, and they are bounded by the absence of the USL. The extent of the USL delineates the zone of transitional frictional behavior.

Silent earthquakes, or episodic slow slip events (SSEs), and nonvolcanic tremor have been observed in a few shallow subduction zones such as Cascadia (*1*–*3*), southwest Japan (*4*–*6*), and southern Mexico (*7*–*15*). In general, most slow slip and tremor activities take place at the transition zone down-dip of the strong coupling section, where great thrust earthquakes occur. In southern Mexico, the Cocos plate is subducting underneath the North America plate, where the slab is almost flat near Guerrero (*16*) and is at a low angle near Oaxaca (Fig. 1) (*17*). SSEs with moment magnitudes M_w of ~7 to 7.5 occur every 1 to 2 years (Fig. 1) (*7*–*11*, *18*, *19*). However, the locations of SSEs vary along-strike, extending about 150 km inland from the Guerrero coast (*7*–*10*, *18*) but are limited to within 100 km near Oaxaca (Fig. 1) (*11*, *15*). In addition, nonvolcanic tremor (NVT) concentrates near the down-dip end of the slow-slip zone (*12*–*14*). This along-strike variation in the location of SSEs and NVT can be compared with the seismic structure of the subducting plate to investigate if the location variation is structurally controlled. We examined locally converted *SP* waves from intraslab earthquakes to map out the seismic structure at the top of the subducting slab beneath southern Mexico (*20*).

SP waves start as shear waves radiated from intraslab earthquakes and convert to *P* waves at the sharp velocity contrast on the plate interface. They are particularly useful for examining a slab structure directly above the source (Fig. 2A) (*21*). The *SP* wave typically arrives 2 to 3 s after the direct *P* wave, depending on the depth of an earthquake (*20*). In this study, we model the first 7 s of the broadband *P* waveforms (0.01 to 0.6 Hz) to explain the interference between the direct *P* wave and the *SP* wave, which ultimately provides a high-resolution map of the upper slab structure (*20*). Our data include two moderate intraslab events recorded by the temporary Meso-American Subduction Experiment (MASE) (*17*) and 40 intraslab events from 1990 to 2008 [body wave magnitude (M_b) = 4.5 ~ 6.0] recorded by the permanent GEOSCOPE station UNM (Fig. 1 and fig. S1).

As an example, we display *P* waveforms recorded at station PTRP and station SAME farther to the north to illustrate how the waveform changes with position (Fig. 2B). The timing of the first negative pulse (pulse A) after the direct *P* wave is consistent with an *SP* arrival, but its amplitude is anomalously large at station PTRP. We can model the *SP* wave that was converted from the bottom of an ultra-slow velocity layer [USL; 3 km and a *S*-wave velocity (V_s) of ~2.7 km/s] directly above the source region. The pulse with a positive polarity (pulse B) immediately following the pulse A is an *SP* arrival converted from the top of the USL. A series of

[1]Department of Terrestrial Magnetism, Carnegie Institution of Washington, 5241 Broad Branch Road N.W., Washington, DC 20015, USA. [2]Seismological Laboratory, Division of Geological and Planetary Science, California Institute of Technology, 1200 East California Boulevard, Pasadena, CA 91125, USA. [3]Department of Geology, Miami University, 114 Shideler Hall, Oxford, OH 45056, USA. [4]Department of Earth and Space Sciences, Center of Embedded Network Systems (CENS), University of California, Los Angeles (UCLA), 595 Charles Young Drive East, Los Angeles, CA 90095–1567, USA. [5]Instituto de Geofísica, Universidad Nacional Autónoma de México, Circuito de la Investigación Científica s/n, Ciudad Universitaria, D.F. 04510 Distrito Federal, México.

*To whom correspondence should be addressed. E-mail: asong@ciw.edu